Analytical assessment of Kelvin-Helmholtz instability growth at Ganymede's upstream magnetopause

*N. Kaweeyanun(1), A. Masters(1), X. Jia(2)

(1) Department of Physics, Imperial College London

(2) The Climate and Space Sciences and Engineering Department, University of Michigan

Corresponding author: N.Kaweeyanun

Corresponding author email: nk2814@ic.ac.uk

Key Points

- We present the first assessment of Kelvin-Helmholtz (K-H) instability on Ganymede's magnetopause without magnetic reconnection effects.
- Ganymede's magnetopause flanks are K-H unstable with faster growth rates on the near-Jupiter flank due to the finite Larmor radius effects.
- K-H vortices should be viable based on the growth rates, but their prevalence is likely suppressed once reconnection effects are considered.

Abstract

Ganymede is the only Solar System moon that generates a permanent magnetic field. Dynamics inside Ganymede's magnetosphere is likely driven by energy-transfer interactions on its upstream magnetopause. Previously in Kaweeyanun et al. (2020), we created a steady-state analytical model of Ganymede's magnetopause and predicted global-scale magnetic

reconnection to occur frequently throughout the surface. Using the same model, this paper provides the first assessment of Kelvin-Helmholtz (K-H) instability growth on the magnetopause in isolation from reconnection effects. The linear K-H instability growth rate is calculated at Ganymede's equatorial magnetopause flank points under the magnetohydrodynamic with finite Larmor radius effect (MHD-FLR) theory, which accounts for inter-flank growth rate asymmetry due to large gyroradii of Jovian plasma ions. The calculation gives growth rates between $\gamma \approx 0.01 - 48\ \ s^{-1}$, with notable enhancement at the equatorial flank point closer to Jupiter. Then, the ideal MHD K-H instability onset condition is evaluated across the entire Ganymedean magnetopause. We find the conditions along both magnetopause flanks to be K-H favorable at all latitudes with growth rates similar to those at respective equatorial flank points. Using Mercury's magnetopause case as a comparison, we determined that nonlinear K-H vortices are viable at Ganymede based on the calculated growth rates, but the vortex growth will likely be suppressed once global reconnection is taken into account.

Plain Language Summary

Jupiter's largest moon Ganymede produces its own magnetic field, which is submerged without mixing inside Jupiter's much larger magnetic field. The two magnetic fields meet along a boundary called the upstream magnetopause, where Jupiter's plasma (energized gas) is forced to flow around Ganymede at considerable speeds. This leads to a type of turbulent motions known as Kelvin-Helmholtz (K-H) instability, which can twist the magnetopause into tightly coiled vortices and inject Jovian plasmas into Ganymede's magnetic field. These injections are thought to drive plasma convection and space weather events (e.g. auroras) near Ganymede. Here we determine potential locations and rates at which K-H instability can grow along an idealized Ganymedean magnetopause surface with no competing interactions

(e.g. magnetic reconnection), using a model previously established in Kaweeyanun et al. (2020). Our results suggest that K-H instability can grow anywhere along both of Ganymede's magnetopause flanks, with slightly faster growth rates on the flank closest to Jupiter. By comparing the growth rates to those on Mercury's magnetopause, where K-H vortices have been abundantly observed, we conclude that K-H vortices should be viable on Ganymede's magnetopause flanks. However, once magnetic reconnection effects are taken into account, K-H vortex growth will likely be strongly suppressed.

Key Words

Ganymede, Kelvin-Helmholtz instability, analytical model, finite Larmor radius effect, magnetohydrodynamic theory

1. Introduction

Between 1996-2000, the Galileo spacecraft performed six flybys of Ganymede, the largest moon of Jupiter and the Solar System, during which evidence of a permanent magnetic field was detected (Kivelson et al., 1996; Gurnett et al., 1996). Ganymede's equatorial surface magnetic field is ~7 times stronger than the ambient Jovian magnetic field, allowing Ganymede to maintain a small distinct magnetosphere inside Jupiter's much larger one (Kivelson et al., 1998; Kivelson et al., 2002). The primary source of Ganymede's magnetic field is thought to be dynamo action inside an Earth-like molten iron core (Anderson et al., 1996; Schubert et al., 1996). The magnetic field is close to dipolar with a ~176° tilt between the magnetic and rotation axes, but the angle varies by a few degrees between Galileo flybys (Kivelson et al., 2002). The dipole tilt variation may be explained by non-negligible higher order (e.g. quadrupole) moments in Ganymede's permanent magnetic field, or more likely a large subsurface ocean whose convection generates a secondary induced magnetic field

(Kivelson et al., 2002). This potential water presence makes Ganymede a primary destination for the upcoming JUpiter ICy moon Explorer (JUICE) space mission (Grasset et al., 2013).

The Jovian magnetosphere around Ganymede is significantly populated by plasma released from Io's volcanoes. The plasma diffuses outward over time, while rotating in the same direction as Jupiter's rotation, to form a ~3 R_J (R_J = 71,492 km) thick plasma sheet centered around the Jovian centrifugal equator (Kivelson et al., 2004). This plane is tilted ~7° with respect to Ganymede's orbit, which lies close to Jupiter's geographical equator plane, so the moon experiences large variations in plasma and magnetic conditions as it moves up and down through the plasma sheet (Kivelson et al., 2004). At Ganymede's average orbital distance of 15 R_J, the Jovian plasma consists primarily of heavy oxygen and sulfur ions with only 10% contribution from protons – a sharp contrast from the proton-dominated solar wind (Bagenal et al., 2016). Furthermore, the Jovian plasma flow speed near Ganymede is sub-Alfvénic (i.e. magnetic pressure dominant) which leads to a cylindrical magnetosphere (Neubauer, 1998), unlike the super-Alfvénic (i.e. dynamic pressure dominant) solar wind that create bullet-shaped planetary magnetospheres (Neubauer, 1990). The environment around Ganymede hence provides a unique laboratory to study plasma and magnetic interactions in the Solar System.

Based on the magnetic topology, Ganymede's magnetosphere can be divided into "open-field" and "closed-field" regions. The open-field region includes most of Ganymede's polar caps. In this region, each magnetic field line connects from one of Ganymede's magnetic poles to the corresponding Jupiter's magnetic poles, forming an extended magnetotail structure known as the Alfvén wings (Neubauer, 1998; Jia, Kivelson et al., 2010). Under magnetohydrodynamic (MHD) theory, plasma particles can enter and escape Ganymede's

magnetosphere along these open field lines, but they do not have sufficiently large number or velocity to influence dynamics inside the magnetosphere (Frank et al., 1997; Williams, Mauk, & McEntire, 1997; Williams, Mauk, McEntire, Roelof et al., 1997). Meanwhile, the closed-field region spans low-latitude areas upstream and downstream of Ganymede, in which each magnetic field line has both ends at Ganymede's magnetic poles. On the upstream side, the outermost closed magnetic field lines are compressed by ambient Jovian magnetic field lines along a boundary known as the upstream magnetopause. Dynamics inside Ganymede's magnetosphere are likely driven by interactions on the upstream magnetopause, similar to a Dungey cycle in planetary magnetospheres (e.g. Jia, Walker et al., 2010; Collinson et al., 2018). Two of the most commonly studied magnetopause interactions are magnetic reconnection and Kelvin-Helmholtz (K-H) instability. We have previously investigated global magnetic reconnection at Ganymede's upstream magnetopause in Kaweeyanun et al. (2020), therefore this paper will focus on the role of K-H instability in energy transport into Ganymede's magnetosphere.

K-H instability arises from bulk flow shear between plasmas just outside and inside a magnetopause boundary. The instability can be divided into two distinct phases – a linear phase in which the magnetopause develops wavelike oscillations (e.g. Dungey, 1955; Southwood, 1968), followed by a nonlinear phase in which the waves grow into turbulent vortices (e.g. Southwood, 1979; Miura, 1982). The nonlinear phase is particularly important as multiple plasma/magnetic layers become tightly wound inside a K-H vortex, separated by very thin and unstable current sheets. These conditions can facilitate cross-magnetopause energy transport via turbulent decay (Nakamura et al., 2004; Matsumoto & Hoshino, 2006), coupling with kinetic Alfvén waves (Chaston et al., 2007), or inducing local magnetic reconnection (Nykyri & Otto, 2001; Nakamura et al., 2006, 2008). The existence of linear K-

H waves at Ganymede's upstream magnetopause has been speculated from Galileo observations (Kivelson et al., 1998; Volwerk et al., 1999; Volwerk et al., 2013) and a numerical model (Tóth et al., 2016). However, there has not been a focused study on K-H vortices, or general K-H instability growth, at Ganymede's magnetopause.

The assessment detailed in this paper thus relies on K-H instability knowledge gained from previous planetary magnetopause studies. Both K-H waves and vortices have been observed at Earth's magnetopause, with evidence of energy transport in the vortex phase (Fairfield et al., 2000; Owen et al., 2004**;** Hasegawa, Fujimoto, Phan et al., 2004). Similar detections of two K-H instability phases are seen at Saturn's magnetopause (Masters et al., 2009; Masters et al., 2010; Wilson et al., 2012; Delamere et al., 2013), and the instability is predicted for Jupiter's magnetopause (Desroche 2012; Masters 2017; Zhang et al., 2018). Magnetic guide field is found to stabilize K-H instability growth, therefore K-H vortices are expected mainly on magnetopause flanks where magnetosheath and magnetospheric magnetic fields are either parallel or antiparallel (Thomas and Winske, 1993; Miura, 1995**;** Eastwood et al., 2015). Observations suggest K-H vortices strongly favor the parallel magnetic configuration i.e. the interplanetary magnetic field (IMF) is northward (Hasegawa, Fujimoto, Phan et al., 2004; Masters et al., 2010), but smaller intermittent instability growth is viable under the antiparallel configuration i.e. the IMF is southward (Hwang et al., 2011). The latter scenario is particularly important because Ganymede's magnetopause always maintains a near-antiparallel magnetic configuration due to the moon's 176° magnetic axis tilt angle and the dominant southward component of the Jovian magnetic field.

There is a temptation to only use the ideal MHD theory for K-H instability assessment. However, observations from Mercury's magnetopause indicate that kinetic effects can also

play an important role in K-H instability growth. Both K-H linear waves and nonlinear vortices have been observed at Mercury's magnetopause (Slavin et al., 2008; Boardsen et al., 2010; Sundberg et al., 2012; Liljeblad et al., 2014). But unlike other planetary cases, K-H vortices are seen primarily on the dusk flank of Mercury's magnetopause (Sundberg et al., 2012; Liljeblad et al., 2014). The asymmetry is a consequence of the finite Larmor radius (FLR) effect, a kinetic phenomenon in which gyromotions of ions inside near-magnetopause plasmas create vorticities that add to or subtract from bulk flow shear vorticity (Nagano, 1978; Nagano, 1979; Huba, 1996). The FLR effect is particularly enhanced at Mercury as its magnetopause is thin enough that the gyroradii of nearby ions become significant (Glassmeier & Espley, 2006; Sundberg et al., 2010; Nakamura et al., 2010; Paral & Rankin, 2013). As Ganymede's magnetosphere is of similar size to Mercury's, we expect a similarly thin magnetopause therefore FLR effect must be considered when assessing K-H instability growth.

Hence in Section 2, we will first calculate the K-H instability growth rate at Ganymede's upstream magnetopause flanks under MHD-FLR hybrid theory. Then, we will assess K-H instability onset and propagation at global scale under the general ideal MHD theory in Section 3. Both assessments utilize an analytical model which parametrizes plasma/magnetic conditions along an idealized Ganymedean magnetopause surface (Kaweeyanun et al., 2020). The model also assumes that no competing interactions, particularly global-scale magnetic reconnection, occur during this analysis. These simplifications reduce precision of the model's predictions but allow them to be obtained at minimal computational cost. In Section 4, we will compare our results to those on Mercury's magnetopause (where K-H vortices have been observed) to discuss the potential for K-H vortex growth on Ganymede's magnetopause first when reconnection effects are excluded, and later when they are included.

2. K-H Instability Growth Rate Under MHD-FLR Theory

Figure 1 shows a schematic diagram for K-H instability growth on Ganymede's magnetopause flanks in a Cartesian coordinate system centered at Ganymede (GphiO) where X is parallel to the ambient Jovian plasma flow, Y points toward Jupiter, and Z points approximately toward Ganymede's geographical north pole. In this equatorial plane view, the ambient Jovian plasma ($v_{J,0}$) enters from top of the diagram and is symmetrically deflected by the magnetopause, resulting in equal Jovian-side bulk flow velocities (v_J) along both magnetopause flanks. For planetary magnetopauses, the flanks are typically defined as dawn and dusk where the planet rotates in the direction from the dusk flank to the dawn flank. The same geometry does not apply to the Ganymedean system, however, as the Jovian plasma rotates around Jupiter while the solar wind travels radially away from the Sun. Instead, the rotational flow creates "near-Jupiter" and "far-Jupiter" magnetopause flanks where the former lies between Ganymede and Jupiter. If we assume flank-symmetric Ganymedean-side bulk flow velocities (v_G) resulting from the global-scale Dungey-type reconnection (e.g. Jia et al., 2009), then bulk flow shears ($v_{sh} = v_J - v_G$) create equal vorticities (black circular arrows) that point southward (into page) on near-Jupiter flank and northward (out of page) on far-Jupiter flank.

To consider the FLR effect, we choose one point along each flank where ($X = 0$, $Z = 0$). Zoom windows in Figure 1 show local plasma ion gyromotions at these equatorial flank points. Here we assume adjacent Jovian and Ganymedean magnetic fields to be directly southward and northward respectively. Since both magnetic fields never deviate beyond 45° from the Z-axis, the assumption represents a fairly typical magnetic configuration near Ganymede's magnetopause (Khurana 1997; Kivelson et al., 1998; Jia et al., 2008). Near each

flank point, ion gyromotions create Jovian-side ($v_{i,J}$) and Ganymedean-side ($v_{i,G}$) ion flows, where $v_{i,J} \gg v_{i,G}$ as a typical Jovian plasma ion has a much larger gyroradius and a smaller gyrofrequency (shown later in Table 1). The resulting ion flow shears ($v_{i,sh} = v_{i,J} - v_{i,G}$) are therefore significant and create equal southward vorticities (red circular arrows) on both near-Jupiter and far-Jupiter flanks. Since the plasma bulk flow and ion gyromotion-related flow vorticities are parallel on the near-Jupiter flank but antiparallel on the far-Jupiter flank, the combined vorticity must be greater on the near-Jupiter flank, so the K-H instability should grow faster on this flank as well.

The K-H instability can be quantified by the growth rate (γ) of its linear wave amplitudes, which we calculate at each magnetopause flank point following (Nagano, 1978, 1979; Sundberg et al., 2010)

$$\gamma = \sqrt{-\frac{\left(\rho_G \nu_G - \rho_J \nu_J\right)^2}{\left(\rho_G + \rho_J\right)^2} k^4 - \frac{2\rho_G \rho_J}{\left(\rho_G + \rho_J\right)^2} (v_{sh}) k^3 + \frac{\rho_G \rho_J}{\left(\rho_G + \rho_J\right)^2} (v_{sh})^2 k^2} \quad \#(1)$$

where ρ is plasma mass density and ν is gyro-viscous coefficient calculated from ion gyroradius R and gyrofrequency Ω. Subscripts "J" and "G" refer to Jovian-side and Ganymedean-side locations respectively. v_{sh} is again the cross-magnetopause bulk flow shear. Lastly, $k = \frac{2\pi}{\lambda}$ is the wavevector corresponding to linear K-H wavelength λ on the magnetopause surface.

Gyro-viscous coefficients and the bulk flow shear can be positive or negative, despite their listed formulas giving only positive magnitudes. At both flank points, we define $\nu_J > 0$ as the Jovian-side ion gyrates with northward rotation vector in Figure 1, and $\nu_G < 0$ as the Ganymedean-side ion gyrates with southward rotation vector. Similarly, we define $v_{sh} < 0$

on near-Jupiter flank and $v_{sh} > 0$ on far-Jupiter flank as bulk flow vorticity vectors are northward and southward there respectively. The value of each negative parameter is equal to its magnitudes multiplied by -1.

K-H instability can grow along a magnetopause flank only if γ is real and positive. The k^4 term is always negative therefore it stabilizes K-H growth at shorter wavelengths. The term depends on ρ and ν, whose values are the same between near-Jupiter and far-Jupiter flanks, so the k^4 term is equal for both flanks. The k^2 term is always positive therefore it encourages K-H instability growth at longer wavelengths. Since this term depends only on ρ and $(v_{sh})^2$, its value is also equal for both flanks. Hence, the FLR effect arises only from the k^3 term, whose value can be positive or negative depending on the sign of linear v_{sh}, which differs between the near-Jupiter and far-Jupiter flanks.

In this study, we consider Jovian plasma to be one singly charged fluid with 14 mass-to-charge (M/Q) ratio, 60 eV temperature, and 4 cm^{-3} number density on both magnetopause flanks (Kivelson et al., 2004). Across the magnetopause, previous studies suggest Ganymedean plasma is also a singly charged fluid with 16 M/Q ratio (O^+ dominant), 1.0 eV temperature, and 2 cm^{-3} number density on both flanks (Eviatar and Vasyliunas, 2001; Jia et al., 2008; Jia et al., 2009). The estimated magnetic field strengths on Jovian and Ganymedean sides of each magnetopause flank are 67 nT and 122 nT respectively (derived from analytical model results in Figures 4e-4f later discussed in Section 3). Hence, we calculate the ion gyroradius, gyrofrequency, and gyro-viscous coefficient on both sides of the magnetopause in Table 1. The Jovian ion gyroradius (62.91 km) is non-negligible compared to Ganymede's magnetopause current sheet thickness (<400 km from Kivelson et al., 1998), justifying inclusion of the FLR effect in K-H instability growth rate calculations.

The ambient Jovian plasma flows at a typical speed of $v_{J,0} \approx 140$ km/s (Williams, Mauk, & McEntire, 1997; Williams, Mauk, McEntire, & Roelof, et al., 1997; Jia et al., 2008). As the ambient plasma approaches Ganymede's magnetosphere, it first slows down near the nose of the upstream magnetopause and then accelerates near the magnetopause flanks due to Bernoulli's effect (e.g. Jia et al., 2009). Therefore, we consider a range of Jovian flow speed between $v_J = 100 - 200$ km/s with 1 km/s resolution in this study. In comparison, the antiparallel Ganymedean plasma flow speed is taken to be negligible $v_G \approx 0$ km/s. This is a viable assumption because our idealized model does not consider plasma/magnetic interactions inside Ganymede's magnetosphere e.g. magnetic reconnection in the downstream magnetotail. Hence, the bulk flow shear $v_{sh} \approx v_J$ is effectively an independent variable.

Another variable is the K-H wavelength λ. The Galileo spacecraft measures near-magnetopause magnetic perturbation periods of 15-20 s, which gives $\lambda \sim 1050 - 1400$ km assuming K-H waves propagate at $v_p \sim 0.5 v_{sh} \sim 0.5 v_J$ (Kivelson et al., 1998). However, the K-H wavelength remains poorly constrained given lack of published plasma data during magnetopause crossings from Galileo, so we choose an extended range of $\lambda = 0 - 30{,}000$ km with 1 km resolution for our study. This range is also consistent with one used in Sundberg et al. (2010) K-H instability growth rate study at Mercury's magnetopause, to which we will compare our results in Section 4.

Figure 2 shows the logarithm of K-H instability growth rate at near-Jupiter and far-Jupiter equatorial flank points with respect to the bulk flow shear and the logarithm of linear K-H wavelength (normalized in R_G for later Ganymede-Mercury comparison). The minimum K-H wavelength thresholds for positive growth rate is between 10-19 km on near-Jupiter flank and 38-76 km on far-Jupiter flank. The threshold value at $v_{sh} = 100$ km/s is approximately twice of value at $v_{sh} = 200$ km/s, as the K-H wavelength is inversely proportional to bulk flow shear along the zero-growth-rate curve. At a particular flow shear speed on either flank, the growth rate first rises briefly, reaching its peak only a few km after the minimum K-H wavelength threshold, and then monotonically falls as λ continues to increase. The initial growth rate rise is due to significance of the k^4 term on the near-Jupiter flank and the k^3 term on the far-Jupiter flank, while the subsequent fall is due to dominance of the k^2 term in the growth rate expression. Both flanks have minimum growth rates of $\approx$0.01 s^{-1} at longest K-H wavelengths. Maximum growth rates meanwhile significantly diverge, reaching 47.89 ($\approx$ 48) s^{-1} on near-Jupiter flank but only 6.71 ($\sim$7.0) s^{-1} on far-Jupiter flank. Typical Ganymedean K-H wavelengths are confined between two dashed magenta lines. Inside this range, the growth rate is limited to 0.21-0.61 s^{-1} on near-Jupiter flank and 0.20-0.60 s^{-1} on far-Jupiter flank.

The growth rate asymmetry between the two flanks $\Delta\gamma = \gamma_n - \gamma_f$ is shown as a fraction of the far-Jupiter value γ_f in Figure 3. Unlike the actual growth rate values, the asymmetry fraction decreases with faster bulk flow shear. The asymmetry fraction grows as large as $\frac{\Delta\gamma}{\gamma_f} \sim 20$ near the minimum K-H wavelength thresholds and as small as $\frac{\Delta\gamma}{\gamma_f} \sim 0.001$ at longest K-H wavelengths. Typical Ganymedean wavelengths are again denoted by dashed magenta lines, inside which the asymmetry fraction is $\frac{\Delta\gamma}{\gamma_f} = 0.02 - 0.06$.

We test the sensitivity of K-H instability growth rate to the near-magnetopause conditions by changing ion M/Q ratio, temperature, and number density inputs by ±50% on both Jovian and Ganymedean sides of the boundary. The growth rate is found most sensitive to negative changes in the three Jovian-side parameters, with the maximum rate increasing up to ~100 s^{-1} (~2 factor) on the near-Jupiter flank. Within typical Ganymedean K-H wavelengths however, effects of near-magnetopause conditions become effectively negligible. For the growth rate asymmetry, it is difficult to determine the parameter to which the asymmetry fraction is most sensitive. The maximum asymmetry value is not a meaningful measurement as it is almost completely determined by numerical effects. With each parameter change, we generally find that the asymmetry fraction increases/decreases by ~50% at shorter wavelengths close to minimum K-H wavelength threshold. This sensitivity is then reduced to <5% at $\lambda > \sim 100$ km.

Implications of K-H instability growth rates on the formation of nonlinear K-H vortices, and the significance of FLR effect on Ganymede's upstream magnetopause, will be revisited in Section 4.

3. Assessment of K-H Instability Onset across Ganymede's Upstream Magnetopause

As discussed in Section 1, waves on Ganymede's upstream magnetopause may arise from the linear phase of K-H instability. However, the formation of linear K-H waves at Ganymede has not been assessed under fundamental plasma theory. This can be achieved by evaluating

the K-H instability onset condition across Ganymede's magnetopause. Since we are considering a global-scale situation, the ideal MHD onset condition can be used following Masters (2017)

$$\left[\mathbf{k}\cdot\left(\mathbf{v_J}-\mathbf{v_G}\right)\right]^2 > \frac{1}{\mu_0}\left(\frac{1}{\rho_J}+\frac{1}{\rho_G}\right)\left[\left(\mathbf{k}\cdot\mathbf{B_J}\right)^2+\left(\mathbf{k}\cdot\mathbf{B_G}\right)^2\right] \quad \#(2)$$

where **k** is the K-H wavevector of unit length, **v** is bulk flow velocity vector, **B** is magnetic field vector, ρ is plasma mass density, and $\mu_0 = 4\pi \times 10^{-7}$ H/m is the vacuum permeability constant. Subscripts "J" and "G" denote Jovian and Ganymedean sides of the magnetopause respectively. A point on the magnetopause surface is considered "K-H unstable" if the inequality is satisfied. The unstable condition is favored if 1) the bulk flow shear is large, 2) mass densities on both sides of the boundary are large, 3) adjacent magnetic fields are weak, and 4) the K-H wavevector is parallel to the bulk flow shear and/or orthogonal to adjacent magnetic fields.

In this study, Ganymede's magnetopause surface is produced by an analytical model whose construction has been detailed in Kaweeyanun et al., (2020). The model domain in GphiO coordinates is $-4.0 < \mathrm{Y} < 4.0$ $\mathrm{R_G}$ and $-1.0 < \mathrm{Z} < 1.0$ $\mathrm{R_G}$ with 0.01 $\mathrm{R_G}$ resolution in each dimension. The model accounts for Ganymede's up-down movement in the Jovian plasma sheet via Jupiter's east longitude parameter ϕ. The magnetopause is north-south symmetric when Ganymede lies at the center of the Jovian plasma sheet ($\phi = 248°$), and gains largest asymmetry when the moon reaches its highest point ($\phi = 158°$) and lowest point ($\phi = 338°$) in the plasma sheet. We will consider these three specific cases when evaluating the K-H instability onset condition.

The model then parametrizes plasma and magnetic parameters on both sides of the magnetopause. Figure 4 (adapted from Kaweeyanun et al., 2020) demonstrates this process for the case when $\phi = 248°$. The magnetopause is first projected onto a Y-Z plane (bulk flow into page) and the surface X-coordinates shown in Figure 4a. As expected, the magnetopause curves downstream (X value increasing) toward the flanks, where the equatorial flank points used for the K-H instability growth rate calculations in Section 2 are dotted in red. Two dashed lines denote boundaries between open-field and closed-field regions.

The ambient Jovian plasma is assumed to flow at $v_{J,0} \approx 140$ km/s along the X-direction for all Ganymede positions (Jia et al., 2008). Figures 4b depicts plasma bulk flow velocity ($\mathbf{v_J}$) on the Jovian-side magnetopause for $\phi = 248°$. The flow collides with the magnetopause and the Jovian-side speed (v_J) is parametrized as a sine function of the flaring angle between the local magnetopause normal and the ambient flow direction (Kaweeyanun et al., 2020). Hence, the flow speed is slower near the subflow point ($Y = 0, Z = 0$) where the collision is head-on, and higher along the flanks where the flow is less impeded by the magnetopause. Normalized arrows indicate Jovian-side flow directions consistent with plasma traversing around Ganymede along the magnetopause surface (Kaweeyanun et al., 2020).

The ambient Jovian plasma mass density depends on Ganymede's position in the plasma sheet, maximized at $\rho_{J,0} = 56$ amu/cm^{-3} when $\phi = 248°$ and minimized at $\rho_{J,0} = 28$ amu/cm^{-3} when $\phi = 158°, 338°$ (Kivelson et al., 2004; Jia et al., 2008). Figure 4c shows the

Jovian-side mass density (ρ_J) when $\phi = 248°$. The Jovian-side mass density is parametrized as a cosine function of the flaring angle with a positive offset equal to the ambient density, as the plasma gains density from magnetopause collision (Kaweeyanun et al., 2020). The density is highest near the subflow point where head-on collision creates largest plasma compression, and lowest near the flanks where the compression is negligible. The value $\rho_J \approx 56$ amu/cm^3 at the flanks is consistent with mass density used in Section 2.

The combined thermal and energetic plasma pressure of the ambient Jovian plasma is $P_{J,0} = 3.8$ nPa when $\phi = 248°$ and $P_{J,0} = 1.9$ nPa when $\phi = 158°, 338°$ (Kivelson et al. 2004; Jia et al., 2008). Figure 4d shows the Jovian-side plasma pressure (P_J) when $\phi = 248°$. Like the mass density, the pressure increase from near-magnetopause compression is parametrized as a cosine relation of the flaring angle and added to the ambient values, resulting in higher pressure near the subflow point and lower pressure along the flanks (Kaweeyanun et al., 2020).

In our model, the ambient magnetic field carried by the Jovian plasma has strength $B_{J,0} = 70$ nT when $\phi = 248°$ and $B_{J,0} = 105$ nT when $\phi = 158°, 338°$ (Khurana, 1997; Jia et al., 2008). Assuming negligible $B_{J,0,x}$ component (Jia et al., 2008), the ambient Jovian field strength is distributed between $B_{J,0,y}$ and $B_{J,0,,z}$ components such that the field points along negative Z-direction when $\phi = 248°$, and deviates $\approx 45°$ from negative Z-direction when $\phi = 158°, 338°$ (Jia et al., 2008; Kaweeyanun et al., 2020). The magnetic field is compressed near the magnetopause similar to the mass density and plasma pressure, so the Jovian-side field ($\mathbf{B_J}$) is strongest near the subflow point and weakest along the flanks as shown in Figure

4e when $\phi = 248°$. The magnetic field strength is $B_J \approx 67$ nT at both equatorial flank points. The pressure conservation method used to determine the Jovian-side field strength is previously discussed in Kaweeyanun et al., (2020). The Jovian-side field direction (normalized arrows) is similar to the ambient direction, but additionally constrained to be parallel to the magnetopause surface (Kaweeyanun et al., 2020).

Plasma inside Ganymede's magnetosphere exerts negligible pressure due to its relatively cold temperature (Jia et al., 2008). Therefore, Ganymede's magnetic field is the primary contributor in balancing the combined Jovian-side plasma and magnetic pressures adjacent to the magnetopause. This allows computation of the Ganymedean-side magnetic field ($\mathbf{B_G}$) shown in Figure 4f when $\phi = 248°$. As expected, the Ganymedean-side field strength is strongest near the subflow point and weakest along the flanks. The magnetic field strength is $B_G \approx 122$ nT at both equatorial flank points. The field direction (normalized arrows) is required to be approximately dipolar and parallel to the magnetopause (Kaweeyanun et al., 2020). The magnetic field points northward in the closed-field region and southward in the open-field region. The Ganymedean-side mass density and bulk plasma flow speed are taken be uniform with magnitudes $\rho_G = 32$ amu/cm^{-3} and $v_G = 0$ km/s respectively, consistent with information used in Section 2.

Once we obtain the magnetopause conditions exemplified in Figure 4 for all three Ganymede positions, we can evaluate the K-H instability onset condition in the closed-field region where the instability can potentially influence Ganymede's magnetospheric dynamics. At each magnetopause surface point, we first assess the onset condition with the K-H

wavevector parallel to the bulk flow shear ($\mathbf{k} \parallel \mathbf{v_J} - \mathbf{v_G}$), and then reassess the condition after every 1° wavevector rotation. Two criteria are required for a point to be considered K-H unstable. First, the point must have at least one wavevector orientation that satisfies the onset inequality. Second, the point must have at least four neighboring points that satisfy the first criterion. The latter criterion removes the "isolated unstable points" (i.e. inequality satisfied by a smallest margin for only one wavevector orientation) where the K-H instability effectively cannot grow.

At each K-H unstable point, we calculate the zero-momentum (center-of-mass) frame velocity along which the K-H linear wave propagates following

$$\mathbf{v_p} = \left(\frac{\rho_J}{\rho_J + \rho_G}\right)\mathbf{v_J} \#(3)$$

where the parameters retain their usual definitions. Since we consider one cross-magnetopause volume containing both Jovian-side and Ganymedean-side plasmas, mass densities can substitute for masses in the velocity expression. The equation indicates that K-H waves always propagate in same direction as the external Jovian-side bulk flow.

Figure 5 shows the K-H instability onset condition assessment in the closed-field region for (a) $\phi = 248°$, (b) $\phi = 158°$, and (c) $\phi = 338°$. Magnetopause conditions are K-H unstable in the colored regions and K-H stable in the white regions. The color scale and normalized arrows describe zero-momentum frame speed and direction respectively. Figure 5a indicates that when Ganymede lies at the center of Jovian plasma sheet, its magnetopause is largely K-

H unstable except the areas immediately north/south of the subflow point. The unstable area includes the magnetopause flanks where the K-H instability growth rates are computed in Section 2 (red dots). The zero-momentum frame speed ranges from <1 km/s closest to the subflow point up to 89 km/s far along the magnetopause flanks.

Figures 5b-5c show sizable reductions in K-H unstable areas as Ganymede is at highest and lowest points relative to the plasma sheet's center. K-H waves can form only inside narrow strips along magnetopause flanks beyond $|Y| > 2$ R_G. The zero-momentum frame speed smaller ranges 50-66 km at these Ganymede positions. We see that the K-H waves can still propagate toward the magnetopause flanks, but with evident effects from the north-south magnetopause asymmetry.

There are two factors why Ganymede's magnetopause become less K-H unstable when $\phi = 158°, 338°$. First, adjacent magnetic fields are 50% stronger compared to when $\phi = 248°$, while Jovian-side mass densities are 50% less dense. Both parameter changes increase the right-hand side of the K-H onset condition thus raising the threshold for K-H instability. The K-H unstable area size is much more sensitive to magnetic field strengths than mass densities as the onset threshold is proportional to $|B_J|^2$ and $\frac{1}{\rho_J}$ respectively. Second, the north-south magnetopause asymmetry means the bulk flow shear is no longer near-orthogonal to the adjacent magnetic fields (which are always strongly antiparallel to each other). Consequently, there exist fewer K-H wavevector orientations that are simultaneously parallel to the bulk flow shear and orthogonal to the adjacent magnetic fields, hence the K-H onset condition is less likely to be satisfied. Sensitivity tests suggest that both factors have

significant impacts on K-H instability onset, but a quantitative impact comparison is difficult due to the approximative nature of our analytical model.

The K-H instability onset is impacted not only by Ganymede's spatial position, but also temporal changes in the Jovian plasma sheet. Although the analytical model assumes steady-state conditions, temporal effects can be mimicked by changing plasma parameters without changing Ganymede's position. Figure 6 illustrates K-H instability onset assessment when the Jovian-side flow speed and mass densities vary by ±50% (magnetic field strengths unchanged due to fixed Ganymede position). The size of K-H unstable area is much more sensitive to the Jovian-side flow speed (Figures 6a-6b) than mass density (Figures 6c-6d), because the left-hand side of the onset condition linearly depends on v_J. But unlike adjacent magnetic fields, increasing the flow speed enlarges K-H unstable areas. Interestingly, the impact of -50% flow speed (Figure 6a) is significantly greater than that of +50% flow speed (Figure 6b). The asymmetry occurs because the bulk flow shear is almost parallel to adjacent magnetic fields directly above/below the subflow point, so the magnetopause is highly K-H stable in these regions.

When $\phi = 248°$, Figure 5a data shows that K-H linear waves propagate at $v_{cm} \sim 0.65v_{sh}$ inside the K-H unstable flank regions. When $\phi = 158°, 338°$, Figures 5b-5c data show the propagation speed is $v_{cm} \sim 0.48v_{sh}$. These values indicate that the assumption $v_p = v_{cm} \sim 0.5v_{sh}$ used to estimate the K-H instability wavelength in Section 2 is reasonable.

4. Discussion

The MHD-FLR theory has previously been applied to calculate K-H instability growth rates at Mercury's equatorial magnetopause flank points (Sundberg et al., 2010). The calculation assumes a directly northward IMF, in which case global magnetic reconnection is minimized. Hence, the Sundberg et al. (2010) model can be compared to our study in Section 2, which also consider Ganymedean K-H instability growth rates without reconnection effects despite the southward Jovian magnetic field orientation. Similar to Figure 2, the Hermean growth rate in Figure 6 of Sundberg et al. (2010) briefly rises and then falls with increasing K-H wavelength for each bulk flow shear speed considered. The growth rates at Mercury's dawn magnetopause flank point are enhanced and of comparable magnitudes to those at Ganymede's near-Jupiter flank point. However, the growth rates on Mercury's dusk flank point are ~1.5 orders of magnitude smaller than those at Ganymede's far-Jupiter flank point. The minimum K-H wavelength thresholds also show larger asymmetry between flanks at Mercury (>1,000 km) than Ganymede (~50 km). Both growth rate and minimum threshold asymmetries suggest a stronger FLR effect at Mercury's magnetopause.

Given their similar scales ($R_G \sim R_M$), the largely comparable K-H instability growth rates between Mercury and Ganymede seem to suggest similar levels of K-H vortex growths. However, this depends on variabilities of typical K-H wavelengths and external magnetic field orientations. On the one hand, K-H vortices grow fastest at shortest K-H wavelengths, therefore a typical Ganymedean wavelength range of 1,050-1,400 km would result in fewer vortices at Ganymede than Mercury, given the latter's estimated wavelength range of 500-5,000 km (Nakamura et al., 2010). On the other hand, Mercury's effective K-H instability growth rates are much lower than MHD-FLR values due to the large range of variabilities of

492 the IMF orientation, which is not the case for Ganymede because the Jovian magnetic field is
493 always strongly southward. What is certain, however, is that K-H vortex growth at
494 Ganymede's magnetopause flank points cannot be ruled out given the evidence of Mercury's
495 K-H vortices in Section 1.

496

497 The MHD-FLR theory does not account for the impact of non-negligible magnetopause
498 current sheet thickness on K-H instability growth. Hence, we also consider Mercury's growth
499 rates that are derived from a two-dimensional kinetic simulation (Nakamura et al., 2010),
500 specifically when the pre-instability magnetopause thickness is similar to the local inertial
501 length as this is the situation at Ganymede's magnetopause (Kaweeyanun et al., 2020). In this
502 case, Figure 7 in Nakamura et al. (2010) shows that the Hermean growth rates exhibit rise-
503 and-fall relationships with K-H wavelengths with significantly less prominent peaks and a
504 noticeable dawn-dusk FLR effect, consistent with MHD-FLR results. However, a more
505 quantitative growth rate comparison is not recommended due to differences between MHD-
506 FLR and kinetic theories.

507

508 As an alternative to Mercury comparisons, Ganymede's K-H instability growth rate can be
509 considered as a parameter controlling K-H wave amplitude such that

$$A_f = A_i e^{\gamma t} \#(4)$$

510 where A_i is the initial amplitude before K-H instability growth and A_f is the final amplitude
511 after time t. A very large K-H wave amplitude is likely to, but not necessarily, induce a K-H
512 vortex as long as the wave has not propagated past Ganymede's magnetotail. We estimate the

distance (in R_G) a K-H wave travels before its amplitude reaches the K-H vortex threshold, taken to be $A_f = 100$ nT, in Table 2 using initial amplitudes $A_i = [1, 5, 10, 15, 20]$ nT and growth rates $\gamma = [0.01, 0.1, 1, 10]$ s^{-1}. A K-H wave is assumed to propagate at $v_p = 85$ km/s (from Figure 5a) during its amplitude growth. Ganymede's magnetotail length from magnetopause flank points is ~7.5-9.0 R_G (Jia, Kivelson et al., 2010). Table 2 suggests that a K-H wave will become a vortex unless both the initial amplitude and the growth rate are small ($A_i < 5$ nT and $\gamma = 0.01$ s^{-1}). Given values inferred from Galileo measurements ($A_i \approx 10 - 20$ nT, $\gamma = 0.20 - 0.61$ s^{-1}) in Kivelson et al., (1998), this simplistic application of K-H instability theory also suggests that formation of K-H vortices is viable at Ganymede's equatorial magnetopause flank points.

The K-H instability onset assessment in Figure 5 shows that the plasma and magnetic field conditions along Ganymede's magnetopause flanks will lead to K-H waves at all latitudes irrespective of Ganymede's spatial positions relative to Jupiter's plasma sheet. Throughout these flank K-H unstable regions, local magnetic shear angles are close to 180° and the bulk flow shears are nearly orthogonal to Jovian/Ganymedean magnetic fields (Kaweeyanun et al., 2020). Consequently, magnetic and plasma configurations are similar to Figure 1 at all flank latitudes for all Ganymede spatial positions, so we can adopt K-H instability growth rates in Section 2 throughout Ganymede's magnetopause flank regions. Figure 5 also indicates that K-H instability occurs more frequently (larger K-H unstable area) when Ganymede lies at center of the Jovian plasma sheet. This is opposite from global-scale magnetic reconnection which occurs more frequently when Ganymede lies at extreme orbital positions (Kaweeyanun et al., 2020).

This raises the question of relative strengths between K-H instability and global reconnection in cross-magnetopause energy transport, particularly whether they alternate according to Ganymede's position relative to the Jovian plasma sheet. Although this question has been investigated for planetary magnetopauses by Masters (2018), the same method does not apply for Ganymede since the moon does not interact with the solar wind. Hence to answer this question, we evaluate how Ganymede's K-H instability growth interacts with global reconnection. Under southward external magnetic field, reconnection events can disrupt K-H instability growth by altering near-magnetopause plasma/magnetic conditions (Nakamura et al., 2020). We consider as an analogue the case of Mercury's magnetopause when the IMF is southward. In-situ observations from the MESSENGER mission find that only 11% of Mercury's K-H vortices occur under southward IMF (Liljeblad et al., 2014), indicating a suppressive impact of Hermean reconnection on K-H instability growth. Mercury's estimated reconnection electric field strength is ~0.3-3 mV/m (Gershman et al., 2016), which is exceeded by Ganymede's typical values of 2 – 20 mV/m (Kaweeyanun et al., 2020; Zhou et al., 2020). As the two magnetospheres are similar in size, reconnection rates can be compared directly via electric field strengths. Therefore, reconnection at Ganymede occurs at higher rates and should have an even larger suppressive impact on K-H instability growth than at Mercury, especially since the Jovian magnetic field is permanently southward at Ganymede. Consequently, we expect few K-H vortices at Ganymede's magnetopause once global reconnection is taken into account, and the latter interaction should be the dominant mean of cross-magnetopause energy transport for all orbital positions of Ganymede.

In a Dungey-type plasma cycle, magnetic reconnection is also expected in the downstream magnetotail. According to numerical simulations, downstream reconnection generates bulk

plasma flow speed $v_G = 20 - 50$ km/s along the Ganymedean-side magnetopause flank, in direction antiparallel to the Jovian-side flow (e.g. Jia et al., 2009). The incorporation of finite v_G reduces the bulk flow shear and thus the K-H instability growth rate. However, both the growth rates and minimum K-H wavelength thresholds remain within the same orders of magnitude as the results in Section 3. Hence, the introduction of downstream reconnection would not change the main conclusions drawn.

Our discussion does not consider impacts of adjacent magnetic field realignments in response to initial K-H instability growth, which can introduce a stabilizing guide effect, or other disruptive factors such as the tearing-mode instability (Chen et al., 1997), pressure rarefaction regions near the magnetopause (Miura, 1995), and ion cyclotron waves (Volwerk et al., 1999; Volwerk et al., 2013). However, these factors are potential subjects for future research on K-H instability growth along Ganymede's upstream magnetopause.

5. Conclusion

Dynamics within Ganymede's unique magnetosphere are thought to be driven primarily by energy-transfer interactions on the moon's upstream magnetopause. One such interaction is the Kelvin-Helmholtz (K-H) instability particularly during its turbulent nonlinear vortex phase. In this paper, we conduct the first assessment of K-H instability growth on Ganymede's magnetopause, using a previously established analytical model to capture the plasma and magnetic conditions near the boundary (Kaweeyanun et al., 2020). The assessment occurs in isolation from global magnetic reconnection effects and is divided into two steps. First, the K-H instability growth rate is calculated at one equatorial point along

584 each of Ganymede's two magnetopause flanks via a modified magnetohydrodynamic with
585 finite Larmor effect (MHD-FLR) theory, which accounts for effects of large Jovian plasma
586 ion gyroradii. Then, we evaluate the ideal MHD K-H instability onset condition to reveal the
587 extent of instability growth at global scale.

588

589 Ganymede's K-H instability growth rate has an estimated range of $\gamma \approx 0.01 - 48\ s^{-1}$, with
590 slightly faster growth rates at the near-Jupiter equatorial flank point. These values are
591 comparable in magnitude to those along Mercury's dawn magnetopause flank, which seems
592 to suggest a similar level of K-H vortex growth between the two bodies, but this remains
593 inconclusive due to poorly constrained wavelengths of linear K-H waves at Ganymede and
594 highly variable interplanetary magnetic field (IMF) orientation at Mercury. Meanwhile, the
595 inter-flank growth rate asymmetry due to the FLR effect is expected to be less pronounced at
596 Ganymede than Mercury.

597

598 The K-H instability onset assessment reveals the entire low-to-mid latitude portion of
599 Ganymede's magnetopause to be largely favorable for instability growth, particularly near
600 the magnetopause flank regions. K-H waves at these locations should grow at similar rates to
601 those at equatorial flank points given similar plasma/magnetic configurations across
602 Ganymede's magnetopause flanks. The instability growth is expected to be more prevalent
603 when Ganymede is at center of the Jovian plasma sheet, which is opposite from global
604 reconnection which favors conditions when Ganymede is at its highest/lowest points relative
605 to the plasma sheet. We determine the relative strengths between the two phenomena by
606 considering their interaction using Mercury's magnetopause as an analogue case. K-H vortex

607 growth is expected to be strongly suppressed by frequent reconnection events, hence the
608 latter interaction should be the dominant energy-transfer mechanism on Ganymede's
609 upstream magnetopause (Jia, Walker et al., 2010; Kaweeyanun et al., 2020; Zhou et al.,
610 2020).

611

612 The conclusions discussed above are largely qualitative due to approximations used in the
613 MHD-FLR theory and Ganymede's analytical model, and our analysis does not account for
614 time variability in K-H instability growth rates. Future work in this area may focus on
615 quantitative analysis of interactions between magnetic reconnection and K-H instability
616 events, and the effects of temporal dynamics on both types of energy-transfer interactions,
617 both of which can help inform the upcoming JUpiter ICy moon Explorer (JUICE) mission.

618

619 **Acknowledgements**

620 NK is supported by a Royal Society PhD Studentship, and AM is supported by a Royal
621 Society University Research Fellowship. Derived data in Figures 2-6 is available in the
622 Imperial College High Performance Computing Service Data Repository (Kaweeyanun,
623 2020b).

Reference

Anderson, J. D., Lau, E. L., Sjogren, W. L., Schubert, G., & Moore, W. B. (1996). Gravitational constraints on the internal structure of Ganymede. Nature, 384 (6609), 541–543. https://doi.org/10.1038/384541a0

Bagenal, F., Wilson, R. J., Siler, S., Paterson, W. R., & Kurth, W. S. (2016). Survey of Galileo plasma observations in Jupiter's plasma sheet. Journal of Geophysical Research: Planets, 121 (5), 871– 894. https://doi.org/10.1002/2016JE005009

Boardsen, S. A., Sundberg, T., Slavin, J. A., Anderson, B. J., Korth, H., Solomon, S. C., & Blomberg, L. G. (2010). Observations of Kelvin-Helmholtz waves along the dusk-side boundary of Mercury's magnetosphere during Messenger's third flyby. Geophysical Research Letters, 37 (12). https://doi.org/10.1029/2010GL043606

Chaston, C., Wilber, M., Mozer, F., Fujimoto, M., Goldstein, M., Acuña, M., . . . Fazakerley, A. (2007, 11). Mode conversion and anomalous transport in kelvin-helmholtz vortices and kinetic alfvén waves at the earth's magnetopause. Physical review letters, 99, 175004. http://doi.org/10.1103/PhysRevLett.99.175004

643 Chen, Q., Otto, A., & Lee, L. C. (1997). Tearing instability, Kelvin-Helmholtz instability,
644 and magnetic reconnection. Journal of Geophysical Research: Space Physics, 102 (A1), 151–
645 161. https://doi.org/10.1029/96JA03144

646

647 Collinson, G., Paterson, W. R., Bard, C., Dorelli, J., Glocer, A., Sarantos, M., & Wilson, R.
648 (2018). New results from Galileo's first flyby of Ganymede: Reconnection-driven flows at
649 the low-latitude magnetopause boundary, crossing the cusp, and icy ionospheric escape.
650 Geophysical Research Letters, 45(8), 3382–3392. https://doi.org/10.1002/2017GL075487

651

652 Delamere, P. A., Wilson, R. J., Eriksson, S., & Bagenal, F. (2013, 2020/07/08). Magnetic
653 signatures of kelvin-helmholtz vortices on Saturn's magnetopause: Global survey. Journal of
654 Geophysical Research: Space Physics, 118 (1), 393–404.
655 https://doi.org/10.1029/2012JA018197

656

657 Desroche, M., Bagenal, F., Delamere, P. A., & Erkaev, N. (2012). Conditions at the expanded
658 Jovian magnetopause and implications for the solar wind interaction. Journal of Geophysical
659 Research: Space Physics, 117(A7). https://doi.org/10.1029/2012JA017621

660

661 Dungey, J. (1955). Electrodynamics of the outer atmosphere. In Physics of the ionosphere,
662 report of the conference held at the cavendish laboratory. Cambridge: The Physical Society.

663

Eastwood, J. P., Hietala, H., Toth, G., Phan, T. D., & Fujimoto, M. (2015). What controls the structure and dynamics of Earth's magnetosphere? Space Science Reviews, 188 (1), 251–286. https://doi.org/10.1007/s11214-014-0050-x

Eviatar, A., M. Vasyliūnas, V., & A. Gurnett, D. (2001). The ionosphere of Ganymede. Planetary and Space Science, 49(3), 327–336. https://doi.org/10.1016/S0032-0633(00)00154-9

Fairfield, D. H., Otto, A., Mukai, T., Kokubun, S., Lepping, R. P., Steinberg, J. T., … Yamamoto, T. (2000). Geotail observations of the Kelvin-Helmholtz instability at the equatorial magnetotail boundary for parallel northward fields. Journal of Geophysical Research: Space Physics, 105 (A9), 21159–21173. https://doi.org/10.1029/1999JA000316

Frank, L. A., Paterson, W. R., Ackerson, K. L., & Bolton, S. J. (1997). Outflow of hydrogen ions from Ganymede. Geophysical Research Letters, 24 (17), 2151–2154. https://doi.org/10.1029/97GL01744

Gershman, D. J., Dorelli, J. C., DiBraccio, G. A., Raines, J. M., Slavin, J. A., Poh, G., & Zurbuchen, T. H. (2016). Ion-scale structure in Mercury's magnetopause reconnection diffusion region. Geophysical Research Letters, 43 (12), 5935–5942. https://doi.org/10.1002/2016GL069163

685

686 Glassmeier, K.-H., & Espley, J. (2006). ULF waves in planetary magnetospheres (Vol. 169;
687 K. Takahashi, Ed.). American Geophysical Union https://doi.org/10.1029/169GM22

688

689 Grasset, O., Dougherty, M. K., Coustenis, A., Bunce, E., Erd, C., Titov, D. V., ... Van Hoolst,
690 T. (2013). JUpiter ICy moons Explorer (JUICE): An ESA mission to orbit Ganymede and to
691 characterise the Jupiter system. Planetary and Space Science, 78, 1–21.
692 http://doi.org/10.1016/j.pss.2012.12.002

693

694 Gurnett, D. A., Kurth, W. S., Roux, A., Bolton, S. J., & Kennel, C. F. (1996). Evidence for a
695 magnetosphere at Ganymede from plasma-wave observations by the Galileo spacecraft.
696 Nature, 384 (6609), 535–537. https://doi.org/10.1038/384535a0

697

698 Hasegawa, H., Fujimoto, M., Phan, T. D., Rème, H., Balogh, A., Dunlop, M. W., ...
699 TanDokoro, R. (2004). Transport of solar wind into Earth's magnetosphere through rolled-up
700 Kelvin–Helmholtz vortices. Nature, 430(7001), 755–758.
701 https://doi.org/10.1038/nature02799

702

703 Huba, J. (1996). The Kelvin-Helmholtz instability: Finite Larmor radius
704 magnetohydrodynamics. Geophysical Research Letters – Geophysical Research Letters, 23.
705 http://doi.org/10.1029/96GL02767

706

707 Hwang, K. J., Kuznetsova, M. M., Sahraoui, F., Goldstein, M. L., Lee, E., & Parks, G. K.
708 (2011). Kelvin-Helmholtz waves under southward interplanetary magnetic field. Journal of
709 Geophysical Research: Space Physics, 116 (A8). https://doi.org/10.1029/2011JA016596

710

711 Jia, X., Kivelson, M. G., Khurana, K. K., & Walker, R. J. (2010). Magnetic fields of the
712 satellites of Jupiter and Saturn. Space Science Reviews, 152(1), 271–305.
713 https://doi.org/10.1007/s11214-009-9507-8

714

715 Jia, X., Walker, R. J., Kivelson, M. G., Khurana, K. K., & Linker, J. A. (2008). Three-
716 dimensional MHD simulations of Ganymede's magnetosphere. Journal of Geophysical
717 Research: Space Physics, 113(A6). https://doi.org/10.1029/2007JA012748

718

719 Jia, X., Walker, R. J., Kivelson, M. G., Khurana, K. K., & Linker, J. A. (2009). Properties of
720 Ganymede's magnetosphere inferred from improved three-dimensional MHD simulations.
721 Journal of Geophysical Research: Space Physics, 114 (A9).
722 https://doi.org/10.1029/2009JA014375

723

724 Kaweeyanun, N. (2020b). (Supplementary Data) Analytical assessment of Kelvin-Helmholtz
725 instability growth at Ganymede's upstream magnetopause. Version 1.0. Imperial College

High Performance Computing Service Data Repository.
http://www.doi.org/10.14469/hpc/7399. Accessed 21 September 2020.

Kaweeyanun, N., Masters, A., & Jia, X. (2020). Favorable conditions for magnetic reconnection at Ganymede's upstream magnetopause. Geophysical Research Letters, 47 (6), e2019GL086228. https://doi.org/10.1029/2019GL086228

Khurana, K. K. (1997). Euler potential models of Jupiter's magnetospheric field. Journal of Geophysical Research: Space Physics, 102(A6), 11295–11306. https://doi.org/10.1029/97JA00563

Kivelson, M., Bagenal, F., Kurth, W., Neubauer, F., Paranicas, C., & Saur, J. (2004). Magnetospheric interactions with satellites (Vol. 1; F. Bagenal, T. Dowling, & W. McKinnon, Eds.). Cambridge University Press.

Kivelson, M. G., Khurana, K. K., Russell, C. T., Walker, R. J., Warnecke, J., Coroniti, F. V., ... Schubert, G. (1996). Discovery of Ganymede's magnetic field by the Galileo spacecraft. Nature, 384 (6609), 537–541. https://doi.org/10.1038/384537a0

Kivelson, M. G., Khurana, K. K., & Volwerk, M. (2002). The permanent and inductive magnetic moments of Ganymede. Icarus, 157 (2), 507–522. https://doi.org/10.1006/icar.2002.6834

Kivelson, M. G., Warnecke, J., Bennett, L., Joy, S., Khurana, K. K., Linker, J. A., . . . Polanskey, C. (1998). Ganymede's magnetosphere: Magnetometer overview. Journal of Geophysi- cal Research: Planets, 103 (E9), 19963–19972. https://doi.org/10.1029/98JE00227

Liljeblad, E., Sundberg, T., Karlsson, T., & Kullen, A. (2014). Statistical investigation of Kelvin-Helmholtz waves at the magnetopause of Mercury. Journal of Geophysical Research: Space Physics, 119(12), 9670– 9683. https://doi.org/10.1002/2014JA020614

Masters, A. (2017). Model-based assessments of magnetic re- connection and Kelvin-Helmholtz instability at Jupiter's magnetopause. Journal of Geophysical Research: Space Physics, 122 (11), 11,154– 11,174. https://doi.org/10.1002/2017JA024736

Masters, A., Achilleos, N., Bertucci, C., Dougherty, M. K., Kanani, S. J., Arridge, C. S., ... Coates, A. J. (2009). Surface waves on Saturn's dawn flank magnetopause driven by the Kelvin–Helmholtz instability. Planetary and Space Science, 57 (14), 1769–1778. https://doi.org/10.1016/j.pss.2009.02.010

766 Masters, A., Achilleos, N., Kivelson, M. G., Sergis, N., Dougherty, M. K., Thomsen, M. F., .
767 . . Coates, A. J. (2010). Cassini observations of a Kelvin-Helmholtz vortex in Saturn's outer
768 magnetosphere. Journal of Geophysical Research: Space Physics, 115(A7).
769 https://doi.org/10.1029/2010JA015351

770

771 Matsumoto, Y., & Hoshino, M. (2004). Onset of turbulence induced by a Kelvin-Helmholtz
772 vortex. Geophysical Research Letters, 31(2). https://doi.org/10.1029/2003GL018195

773

774 Matsumoto, Y., & Hoshino, M. (2006). Turbulent mixing and transport of collisionless
775 plasmas across a stratified velocity shear layer. Journal of Geophysical Research: Space
776 Physics, 111(A5). https://doi.org/10.1029/2004JA010988

777

778 Miura, A. (1982). Nonlinear evolution of the magnetohydrodynamic Kelvin-Helmholtz
779 instability. Phys. Rev. Lett., 49, 779–782. http://doi.org/10.1103/PhysRevLett.49.779

780

781 Miura, A. (1995). Dependence of the magnetopause Kelvin-Helmholtz instability on the
782 orientation of the magnetosheath magnetic field. Geophysical Research Letters, 22(21),
783 2993–2996. https://doi.org/10.1029/95GL02793

784

Nagano, H. (1978). Effect of finite ion Larmor radius on the Kelvin–Helmholtz instability. , 20(2), 149-160. http://doi.org/10.1017/S0022377800021450

Nagano, H. (1979). Effect of finite ion Larmor radius on the Kelvin-Helmholtz instability of the magnetopause. Planetary and Space Science, 27(6), 881–884. https://doi.org/10.1016/0032-0633(79)90013-8

Nakamura, T., Fujimoto, M., & Otto, A. (2006). Magnetic reconnection induced by kelvin-helmholtz instability and the formation of the low-latitude boundary layer. Geophysical Research Letters - GEOPHYS RES LETT, 331. http://doi.org/10.1029/2006GL026318

Nakamura, T., Fujimoto, M., & Otto, A. (2008). Structure of an mhd-scale kelvin-helmholtz vortex: Two-dimensional two-fluid simulations including finite electron inertial effects. Journal of Geophysical Research: Space Physics, 113 (A9). http://doi.org/10.1029/2007JA012803

Nakamura, T., Hayashi, D., Fujimoto, M., & Shinohara, I. (2004). Decay of mhd-scale kelvin-helmholtz vortices mediated by parasitic electron dynamics. Physical review letters, 92, 145001. http://doi.org/10.1103/Phys- RevLett.92.145001

Nakamura, T., Hasegawa, H., & Shinohara, I. (2010). Kinetic effects on the Kelvin-Helmholtz instability in ion-to-magnetohydrodynamic scale transverse velocity shear layers: Particle simulations. Physics of Plasmas, 17. http://doi.org/10.1063/1.3385445

Nakamura, T. K. M., Plaschke, F., Hasegawa, H., Liu, Y. H., Hwang, K. J., Blasl, K. A., & Nakamura, R. (2020). Decay of kelvin- helmholtz vortices at the earth's magnetopause under pure southward imf conditions. Geophysical Research Letters, 47 (13), e2020GL087574. https://doi.org/10.1029/2020GL087574

Neubauer, F. (1998). The sub-Alfvenic interaction of the Galilean satellites with the Jovian magnetosphere (Vol. 103). http://doi.org/10.1029/97JE03370

Neubauer, F. M. (1990). Satellite plasma interactions. Advances in Space Research, 10, 25–38. http://doi.org/10.1016/0273-1177(90)90083-C

Nykyri, K., & Otto, A. (2001). Plasma transport at the magnetospheric boundary due to reconnection in Kelvin-Helmholtz vortices. Geophysical Research Letters, 28(18), 3565–3568. https://doi.org/10.1029/2001GL013239

824 Owen, C., Taylor, M., Krauklis, I., Fazakerley, A., Dunlop, M., & Bosqued, J. (2004).
825 Cluster observations of surface waves on the dawn flank magnetopause. Annales
826 Geophysicae, 22(3). pp. 971-983. ISSN 09927689, 22. http://doi.org/10.5194/angeo-22-971-
827 2004

828

829 Paral, J., & Rankin, R. (2013). Dawn–dusk asymmetry in the Kelvin–Helmholtz instability at
830 Mercury. Nature Communications, 4 (1), 1645. https://doi.org/10.1038/ncomms2676

831

832 Schubert, G., Zhang, K., Kivelson, M. G., & Anderson, J. D. (1996). The magnetic field and
833 internal structure of Ganymede. Nature, 384 (6609), 544–545.
834 https://doi.org/10.1038/384544a0

835

836 Slavin, J., Acun̄a, M., Anderson, B., Baker, D., Benna, M., Gloeckler, G., . . . Zurbuchen, T.
837 (2008). Mercury's magnetosphere after Messenger's first flyby. Science (New York, N.Y.),
838 321, 85–9. http://doi.org/10.1126/science.1159040

839

840 Southwood, D. J. (1968). The hydromagnetic stability of the magnetospheric boundary.
841 Planetary and Space Science, 16, 587-605.

842

Southwood, D. J. (1979). Magnetopause kelvin-helmholtz instability. In Proceedings of magnetospheric boundary layers conference. Noordwijk, the Netherlands.

Sundberg, T., Boardsen, S. A., Slavin, J. A., Anderson, B. J., Korth, H., Zurbuchen, T. H., . . . Solomon, S. C. (2012). Mercury orbital observations of large-amplitude Kelvin-Helmholtz waves at Mercury's magnetopause. Journal of Geophysical Research: Space Physics, 117(A4). https://doi.org/10.1029/2011JA017268

Sundberg, T., Boardsen, S. A., Slavin, J. A., Blomberg, L. G., & Korth, H. (2010). The Kelvin–Helmholtz instability at Mercury: An assessment. Planetary and Space Science, 58(11), 1434–1441. https://doi.org/10.1016/j.pss.2010.06.008

Thomas, V. A., & Winske, D. (1993, 2020/06/18). Kinetic simulations of the Kelvin-Helmholtz instability at the magnetopause. Journal of Geophysical Research: Space Physics, 98(A7), 11425–11438. https://doi.org/10.1029/93JA00604

Tóth, G., Jia, X., Markidis, S., Peng, I. B., Chen, Y., Daldorff, L. K. S., . . . Dorelli, J. C. (2016). Extended magnetohydrodynamics with embedded particle-in-cell simulation of Ganymede's magnetosphere. Journal of Geophysical Research: Space Physics, 121(2), 1273–1293. https://doi.org/10.1002/2015JA021997

Volwerk, M., Jia, X., Paranicas, C., Kurth, W. S., Kivelson, M. G., & Khurana, K. K. (2013). Ulf waves in Ganymede's upstream magnetosphere. Annales Geophysicae, 31(1), 45–59. https://doi.org/10.5194/angeo-31-45-2013

Volwerk, M., Kivelson, M. G., Khurana, K. K., & McPherron, R. L. (1999). Probing Ganymede's magnetosphere with field line resonances. Journal of Geophysical Research: Space Physics, 104(A7), 14729– 14738. https://doi.org/10.1029/1999JA900161

Williams, D. J., Mauk, B., & McEntire, R. W. (1997). Trapped electrons in Ganymede's magnetic field. Geophysical Research Letters, 24(23), 2953–2956. https://doi.org/10.1029/97GL03003

Williams, D. J., Mauk, B. H., McEntire, R. W., Roelof, E. C., Armstrong, T. P., Wilken, B., . . . Murphy, N. (1997). Energetic particle signatures at Ganymede: Implications for Ganymede's magnetic field. Geophysical Research Letters, 24(17), 2163–2166. https://doi.org/10.1029/97GL01931

Zhou, H., Tóth, G., Jia, X., & Chen, Y. (2020). Reconnection-driven dynamics at Ganymede's upstream magnetosphere: 3d global hall MHD and MHD-EPIC simulations. Journal of Geophysical Research: Space Physics, n/a (n/a), e2020JA028162. https://doi.org/10.1029/2020JA028162

885 *Table 1: Gyromotion Properties of Ions near Ganymede's Upstream Magnetopause*

	Gyroradius (km) $\mathbf{R = \frac{M}{QB}\sqrt{\frac{E}{M}}}$	**Gyrofrequency (s^{-1})** $\mathbf{\Omega = \frac{QB}{M}}$	**Gyro-viscous Coefficient (m^2/s)** $\mathbf{\nu = \frac{R^2\Omega}{4}}$
Jovian-side	62.91	0.46	4.51×10^8
Ganymedean-side	4.75	0.73	-4.11×10^6

886 Note: Symbol meanings are as follow: M/Q = mass-to-charge ratio, B = magnetic field
887 strength, E = ion energy. All parameters are in SI units. The gyro-viscous coefficient is
888 negative if the ion gyrates with southward vorticity.

889

Table 2: Distance Travelled by a K-H Wave before Forming a Nonlinear Vortex

A_i (nT)	γ (s^{-1})			
	0.01	**0.1**	**1**	**10**
1	***14.89***	1.49	0.15	0.01
5	***9.68***	0.97	0.10	<0.01
10	7.44	0.74	0.07	<0.01
15	6.13	0.61	0.06	<0.01
20	5.20	0.52	0.05	<0.01

Note: Distances are in R_G. The K-H vortex threshold is $A_f = 100$ nT and the K-H wave propagation speed is $v_p = 85$ km/s. Bold and italicized distance numbers exceed Ganymede's magnetotail length, set to be 9 R_G.

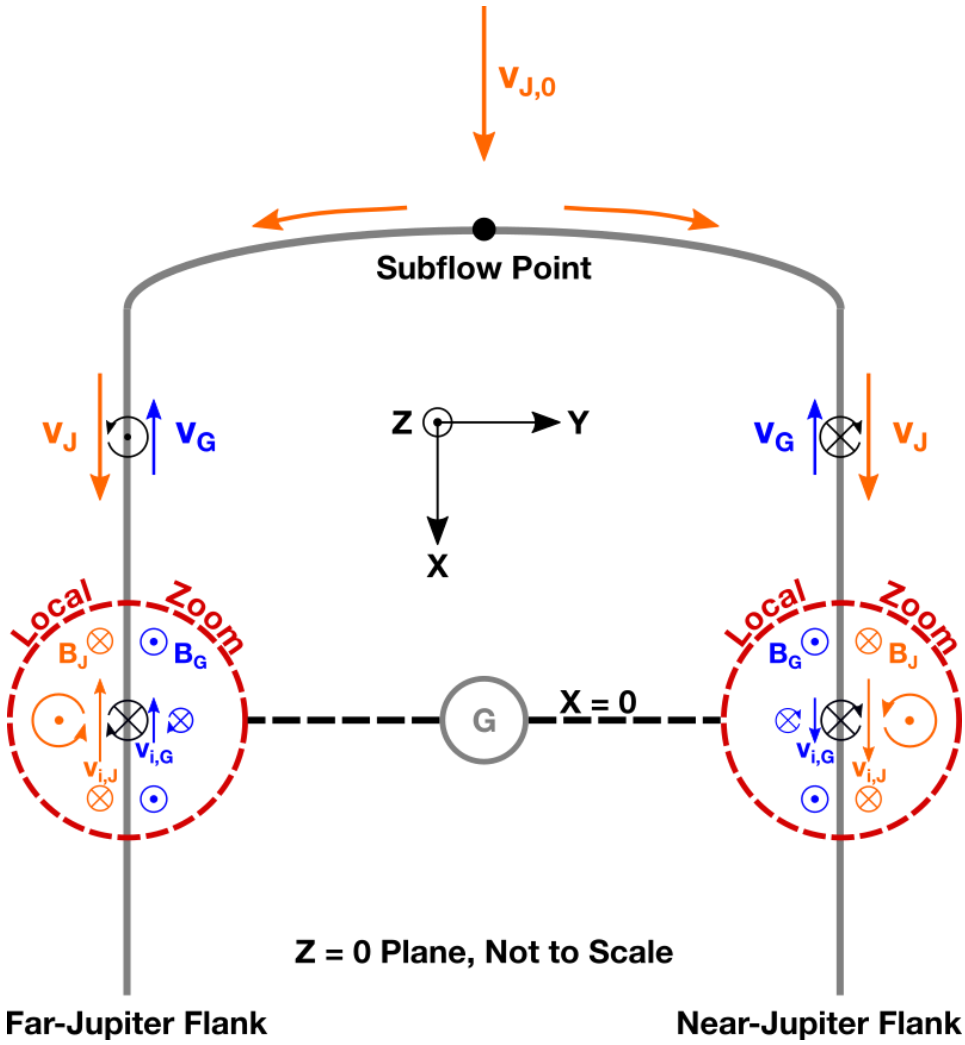

Figure 1: A schematic diagram of K-H instability growth on Ganymede's magnetopause flanks in the equatorial plane of the GphiO coordinate system. Bulk plasma velocities on Jovian (v_J, orange arrows) and Ganymedean (v_G, blue arrows) produce vorticities (black circular arrows) in opposite directions between the two flanks. Local magnetic field orientations (B_J, B_G) and plasma ion gyromotions (orange/blue circular arrows) are shown inside zoom windows (red dashed lines) at ($X = 0$, $Z = 0$) flank points. Subsequent ion velocities on Jovian ($v_{i,J}$, orange arrows) and Ganymedean ($v_{i,G}$, blue arrows) produce ion vorticities (black circular arrows) in the same direction on both flanks. The diagram is not to scale.

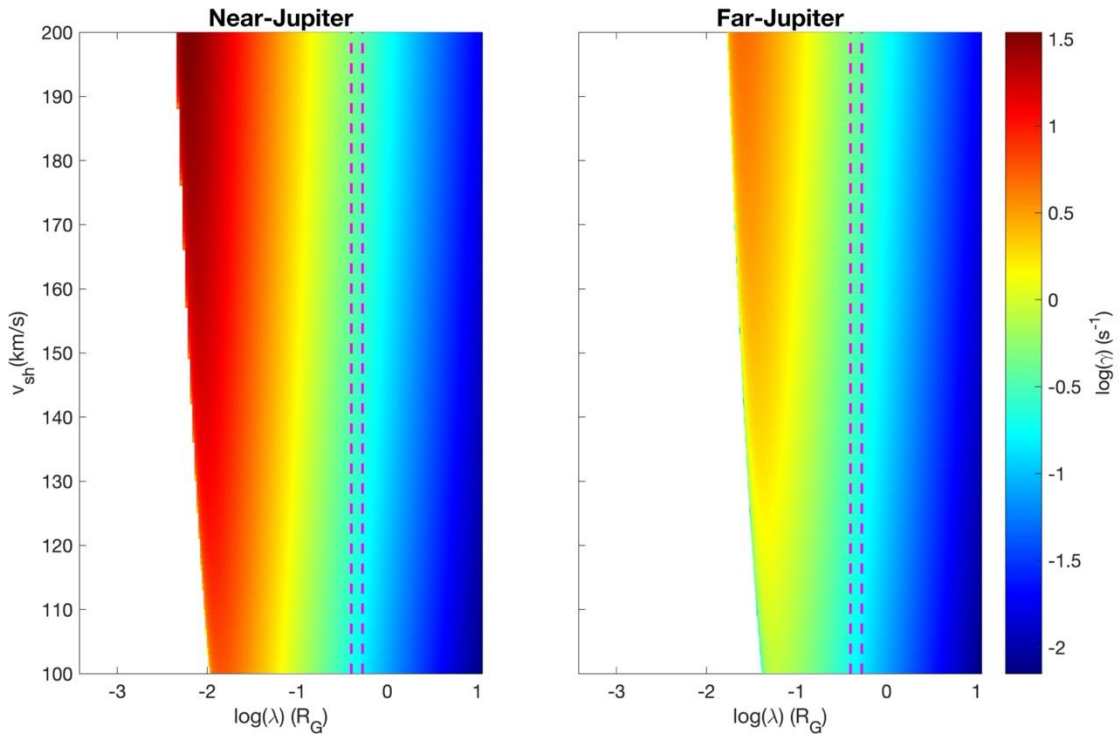

904

905 Figure 2: K-H instability growth rates at Ganymede's near-Jupiter and far-Jupiter equatorial
906 magnetopause flank points, with respect to the logarithm of K-H wavelengths on the
907 horizontal axis and the bulk flow shear on the vertical axis. Typical Ganymedean K-H
908 wavelength ranges are enclosed by dashed magenta lines.

909

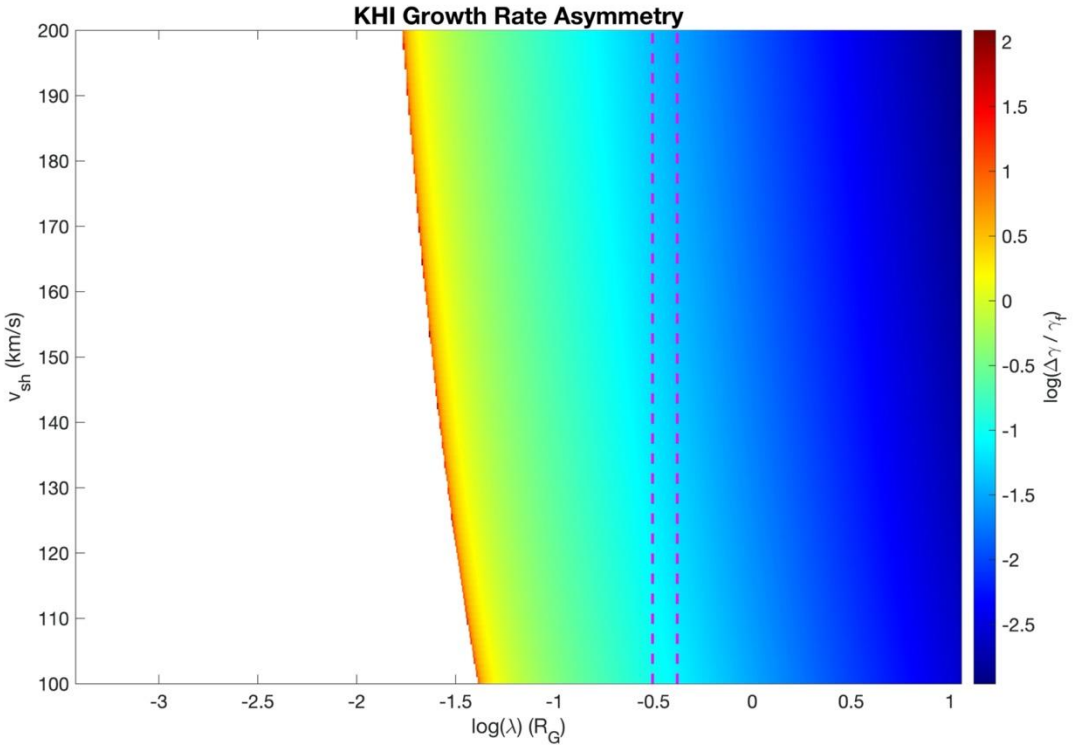

910

911 Figure 3: K-H instability growth rate asymmetry between Ganymede's near-Jupiter and far-
912 Jupiter magnetopause flanks, expressed as a fraction of far-Jupiter growth rate value. The
913 format is the same as Figure 2.

914

915

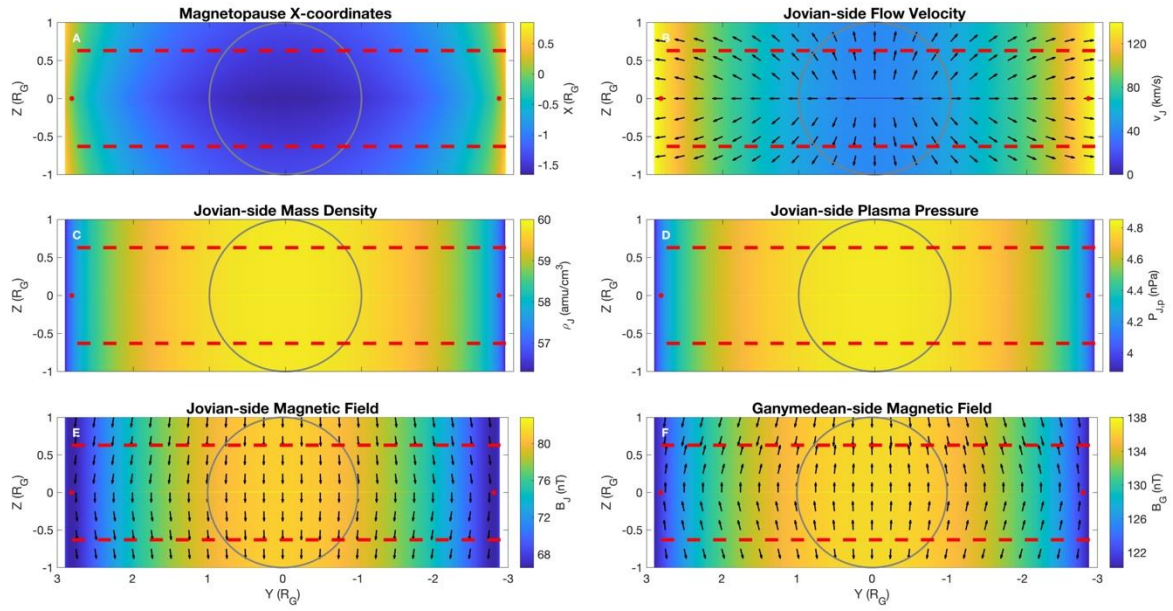

916 Figure 4: Near-magnetopause plasma and magnetic conditions computed by a steady-state
917 analytical model of Ganymede's magnetopause (adapted from Kaweeyanun et al., 2020).
918 Parameters shown are (a) magnetopause X-coordinates, (b) Jovian-side bulk flow velocity,
919 (c) Jovian-side plasma mass density, (d) Jovian-side plasma pressure, (e) Jovian-side
920 magnetic field, and (f) Ganymedean-side magnetic field. In each subplot, the closed-field
921 region between two red dashed lines while the two red dots denote equatorial flank points
922 where K-H instability growth rates are calculated in Section 2. Ganymede is outlined in grey

923

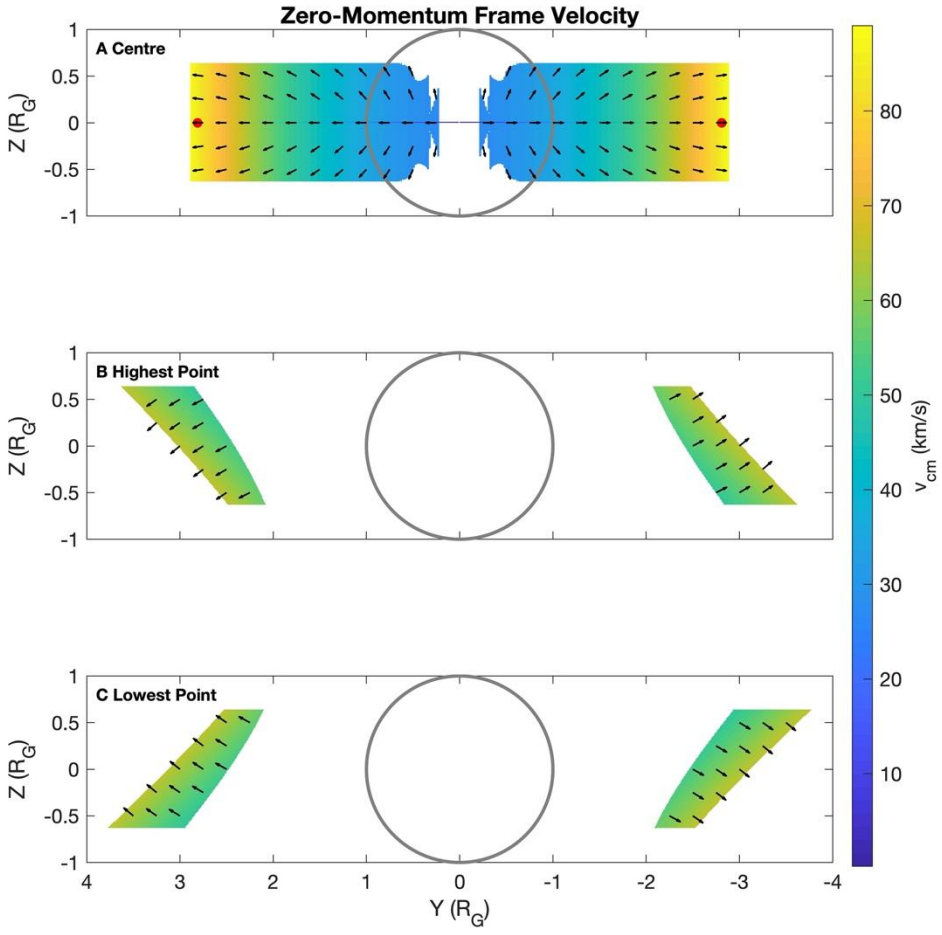

924

925 Figure 5: K-H instability onset assessment when Ganymede lies at (a) center of Jovian
926 plasma sheet and (b/c) highest/lowest points relative to the plasma sheet. K-H unstable
927 locations correspond to colored regions. The shared color bar denotes the speed, and the
928 normalized arrows denotes the direction, of zero-momentum frame velocity for the linear K-
929 H wave. Red dots in Figure 5a show equatorial flank points and Ganymede is outlined in
930 grey.

931

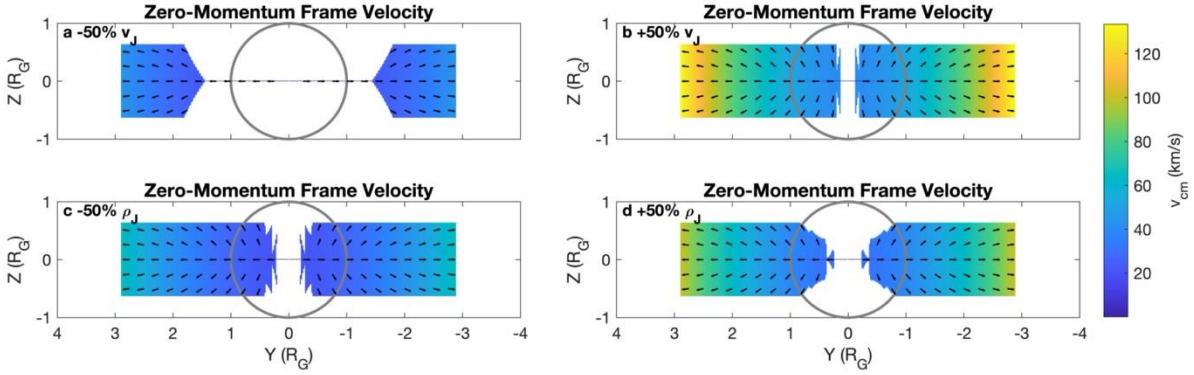

932

933 Figure 6: K-H instability onset assessment when Ganymede lies at center of the Jovian
934 plasma sheet, but with Jovian-side plasma conditions varied to simulate temporal effects.
935 Parameters considered are (a) -50% bulk flow speed, (b) +50% bulk flow speed, (c) -50%
936 mass density, and (d) +50% mass density. The format is the same as Figure 5.

	Gyroradius (km) $\mathbf{R = \frac{M}{QB}\sqrt{\frac{E}{M}}}$	**Gyrofrequency (s^{-1})** $\mathbf{\Omega = \frac{QB}{M}}$	**Gyro-viscous Coefficient (m^2/s)** $\mathbf{\nu = \frac{R^2\Omega}{4}}$
Jovian-side	62.91	0.46	4.51×10^8
Ganymedean-side	4.75	0.73	-4.11×10^6

A_i (nT)	γ (s^{-1})			
	0.01	**0.1**	**1**	**10**
1	***14.89***	1.49	0.15	0.01
5	***9.68***	0.97	0.10	<0.01
10	7.44	0.74	0.07	<0.01
15	6.13	0.61	0.06	<0.01
20	5.20	0.52	0.05	<0.01

Figure 1.

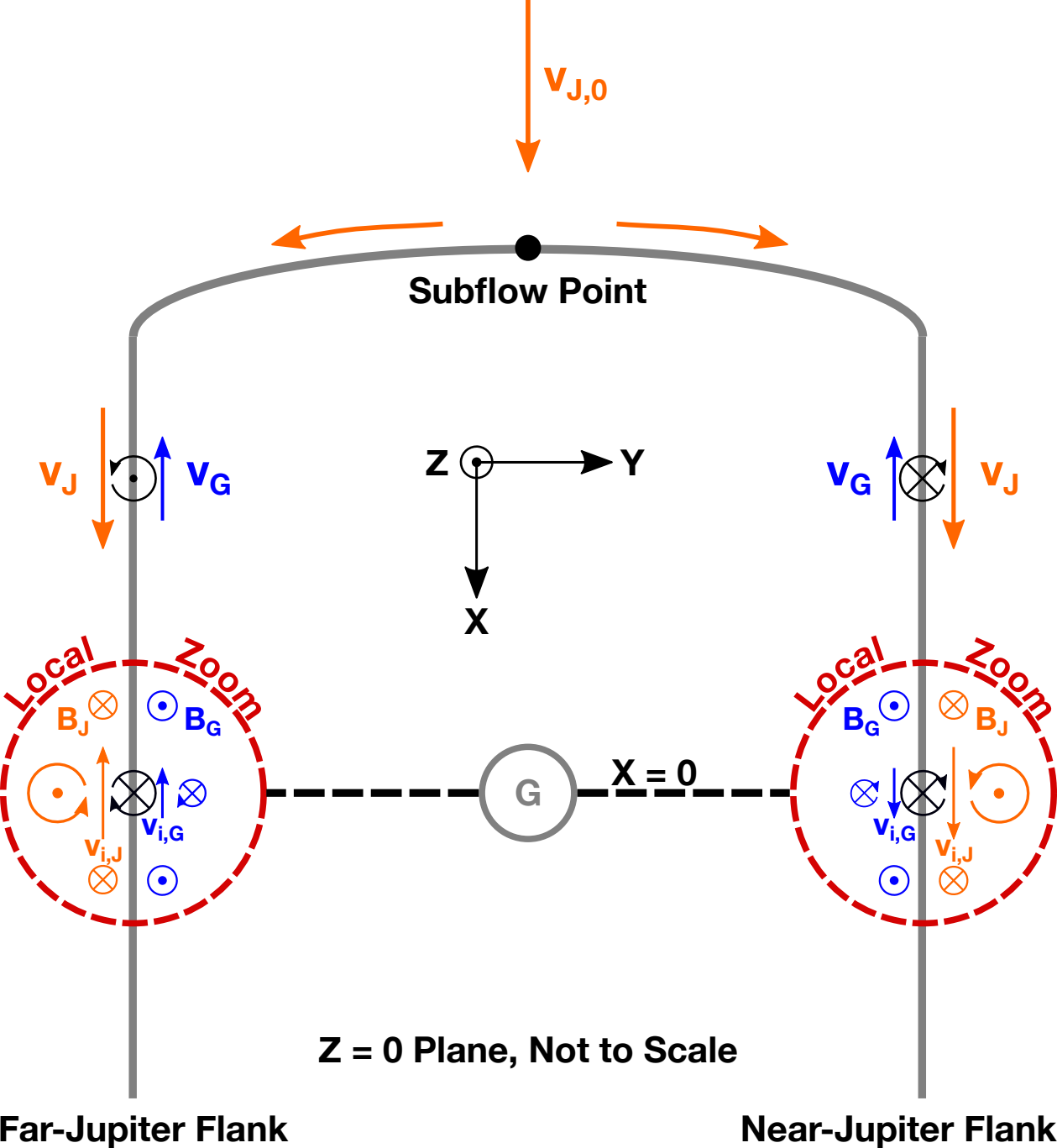
$v_{J,0}$
Subflow Point
v_J
v_G
Z
Y
X
v_G
v_J
Local
Zoom
B_J
B_G
$v_{i,J}$
$v_{i,G}$
G
X = 0
Local
Zoom
B_G
B_J
$v_{i,G}$
$v_{i,J}$
Z = 0 Plane, Not to Scale
Far-Jupiter Flank
Near-Jupiter Flank

Figure 2.

Near-Jupiter

Far-Jupiter

v_{sh} (km/s)

200
190
180
170
160
150
140
130
120
110
100

-3
-2
-1
0
1

log(λ) (R_G)

1.5
1
0.5
0
-0.5
-1
-1.5
-2

log(γ) (s^{-1})

Figure 3.

KHI Growth Rate Asymmetry

v_{sh} (km/s)

200
190
180
170
160
150
140
130
120
110
100

-3
-2.5
-2
-1.5
-1
-0.5
0
0.5
1

$\log(\lambda)$ (R_G)

$\log(\Delta\gamma / \gamma_f)$

2
1.5
1
0.5
0
-0.5
-1
-1.5
-2
-2.5

Figure 4.

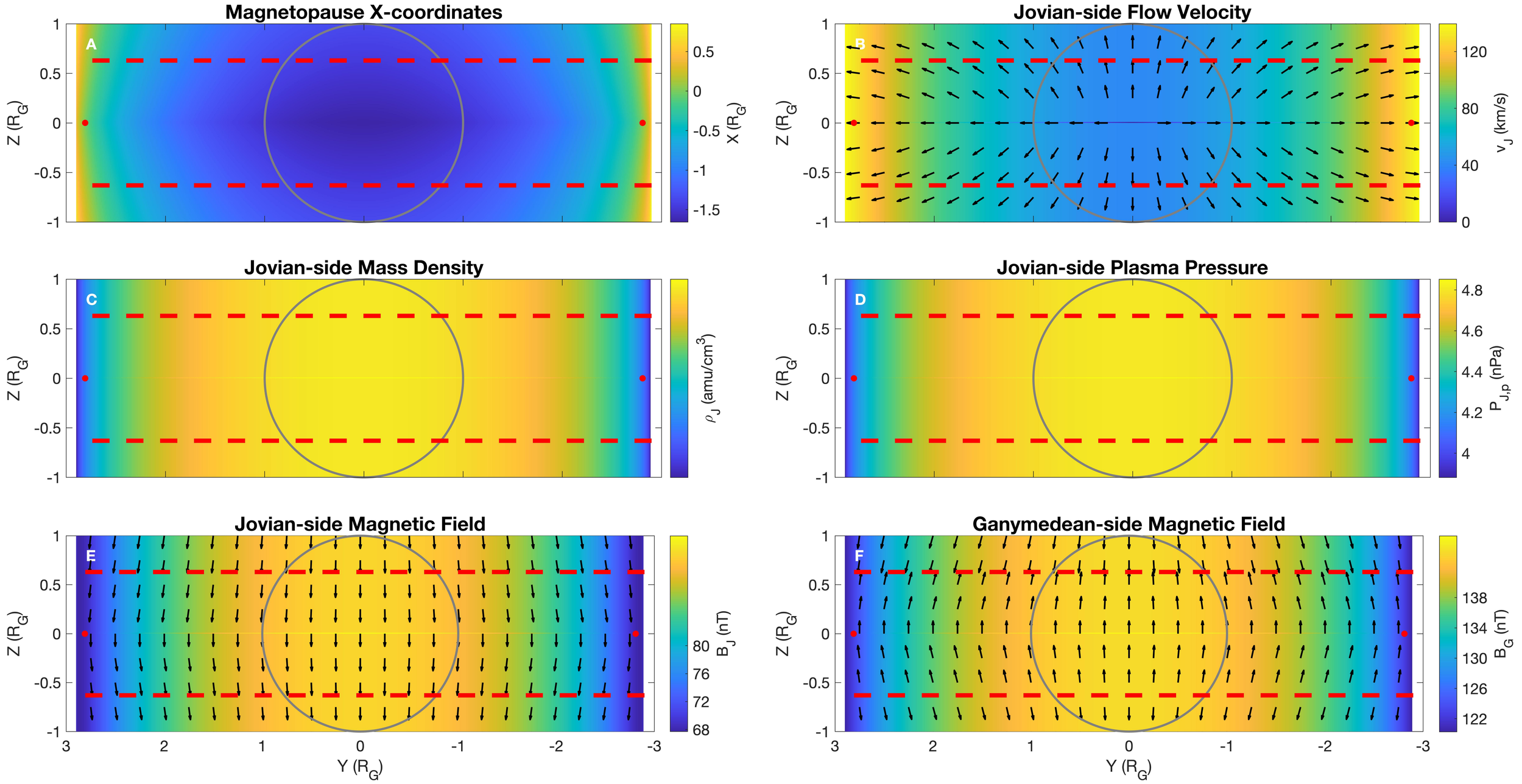
Magnetopause X-coordinates
A
Z (R_G)
X (R_G)
Jovian-side Flow Velocity
B
v_J (km/s)
Jovian-side Mass Density
C
ρ_J (amu/cm^3)
Jovian-side Plasma Pressure
D
P_J,p (nPa)
Jovian-side Magnetic Field
E
B_J (nT)
Ganymedean-side Magnetic Field
F
B_G (nT)
Y (R_G)

Figure 5.

Zero-Momentum Frame Velocity

A Centre

B Highest Point

C Lowest Point

Z (R_G)

Y (R_G)

v_{cm} (km/s)

Figure 6.

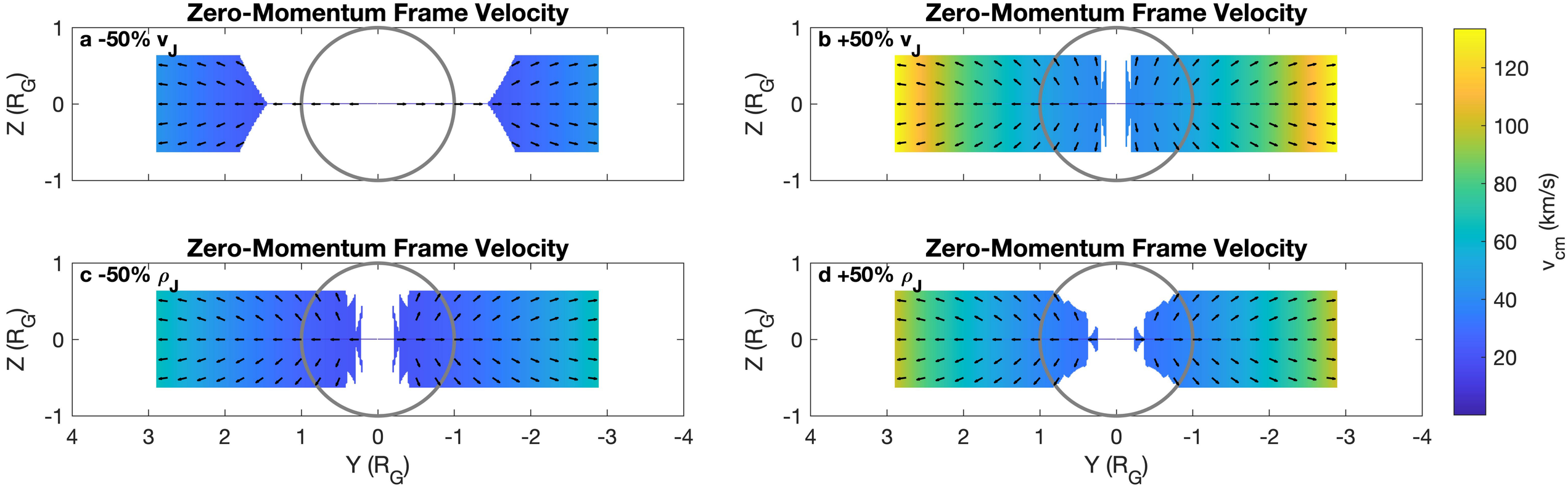
Zero-Momentum Frame Velocity
a -50% v_J
b +50% v_J
c -50% ρ_J
d +50% ρ_J
Z (R_G)
Y (R_G)
v_cm (km/s)
1
0
-1
4
3
2
1
0
-1
-2
-3
-4
120
100
80
60
40
20